Physics in Medicine and Biology

ACCEPTED MANUSCRIPT

Performance evaluation of the PET component of a hybrid PET/CT-ultrafast ultrasound imaging instrument

To cite this article before publication: Mailyn Pérez-Liva *et al* 2018 *Phys. Med. Biol.* in press https://doi.org/10.1088/1361-6560/aad946

Manuscript version: Accepted Manuscript

Accepted Manuscript is “the version of the article accepted for publication including all changes made as a result of the peer review process, and which may also include the addition to the article by IOP Publishing of a header, an article ID, a cover sheet and/or an ‘Accepted Manuscript’ watermark, but excluding any other editing, typesetting or other changes made by IOP Publishing and/or its licensors”

This Accepted Manuscript is **© 2018 Institute of Physics and Engineering in Medicine**.

During the embargo period (the 12 month period from the publication of the Version of Record of this article), the Accepted Manuscript is fully protected by copyright and cannot be reused or reposted elsewhere.
As the Version of Record of this article is going to be / has been published on a subscription basis, this Accepted Manuscript is available for reuse under a CC BY-NC-ND 3.0 licence after the 12 month embargo period.

After the embargo period, everyone is permitted to use copy and redistribute this article for non-commercial purposes only, provided that they adhere to all the terms of the licence https://creativecommons.org/licences/by-nc-nd/3.0

Although reasonable endeavours have been taken to obtain all necessary permissions from third parties to include their copyrighted content within this article, their full citation and copyright line may not be present in this Accepted Manuscript version. Before using any content from this article, please refer to the Version of Record on IOPscience once published for full citation and copyright details, as permissions will likely be required. All third party content is fully copyright protected, unless specifically stated otherwise in the figure caption in the Version of Record.

View the article online for updates and enhancements.

This content was downloaded from IP address 196.11.235.237 on 10/08/2018 at 08:07

Performance evaluation of the PET component of a hybrid PET/CT-Ultrafast Ultrasound Imaging instrument

Mailyn Perez-Liva[1], Thomas Viel[1,2], Thulaciga Yoganathan[1,2], Anikitos Garofalakis[1], Joevin Sourdon[1], Caterina Facchin[1], Mickael Tanter[3], Jean Provost[3] and Bertrand Tavitian[1,2].

[1]Inserm UMR970, Paris Cardiovascular Research Center, Paris, France.

[2]Faculté de Médecine, Université Paris Descartes, Sorbonne Paris Cité, Paris, France.

[3]Institut Langevin, Ecole Supérieure de Physique et de Chimie Industrielles, Paris Sciences and Letters Research University CNRS UMR 7587 Inserm U979, Inserm Technology Research Accelerator in Biomedical Ultrasound, Paris, France.

Abstract:

We recently introduced a hybrid imaging instrument, PETRUS, based on a combination of Positron Emission Tomography (PET) for molecular imaging, X-ray Computed Tomography (CT) for anatomical imaging, co-registration and attenuation correction, and Ultrafast Ultrasound Imaging (UUI) for motion-correction, hemodynamic and biomechanical imaging. In order to ensure a fine co-registration of simultaneous PET-UUI acquisitions, ultrasound probes attached to an ultrafast ultrasound scanner are operated in the field of view (FOV) of a small animal PET/CT scanner using a remote-controlled micro-positioner. Here we explore the effect of the presence of ultrasound probes on PET image quality. We compare the performance of PET and image quality with and without the presence of probes in the PET field of view, both in vitro following the NEMA-NU-4-2008 standard protocol, and in vivo in small animals. Overall, deviations in the quality of images acquired with and without the ultrasound probes were under 10 % and under 7 % for the NEMA protocol and in vivo tests, respectively. Our results demonstrate the capability of the PETRUS device to acquire multimodal images in vivo without significant degradation of image quality.

1. Introduction

To produce images of biological tissues in intact living organisms non-invasively and non-destructively, in vivo imaging techniques measure the interaction between biological tissues and a source of energy specific for the imaging modality. For a given imaging modality, the band of electromagnetic or mechanical energy in play is relatively narrow (Prince and Links, 2006, Enderle and Brozino, 2012) and consequently, the resulting images depict a narrow band of interaction with living tissues and report on a limited number of biological parameters. In contrast, understanding of complex diseases such as cancer or ischemic disorders require a combination of multiple biological parameters, ideally co-registered in space and time. To this end, modern imaging instruments combine several techniques in the same device, such as Positron Emission Tomography-Computed Tomography (PET-CT) (Beyer et al., 2000), Single Photon Computerized Tomography - CT (SPECT-CT) (Hasegawa et al., 2002) or PET – Magnetic Resonance Imaging (MRI) (Schmand et al., 2007, Judenhofer et al., 2008). This increases their cost, complexity, lengthens imaging time, complicates co-registration of image volumes and more importantly, often degrades the image quality of one or of both modalities involved.

We recently introduced PETRUS (**PET R**egistered **U**ltrafast **S**onography; Provost et al., 2018), a hybrid imaging instrument based on simultaneously acquired PET/CT and Ultrafast Ultrasound Imaging (UUI), an ultrasonic imaging method in rapid evolution with numerous biomedical applications (Mace et al., 2011, Errico et al., 2015, Sieu et al., 2015, Osmanski et al., 2014, Tanter and Fink, 2014). We showed that PETRUS yields unprecedented multiparametric information for preclinical oncology and cardiology studies (Provost et al., 2018). However, in the PETRUS embodiment, simultaneous recording of molecular information from PET with functional and anatomical information from UUI is done by controlling the position and movement of an ultrasound probe inside the PET gantry. It is well known that the presence of objects attenuating the 511 keV gamma-rays of positron annihilation inside a PET gantry degrades image quality and creates artifacts in the reconstructed images (Goerres et al., 2003, Sureshbabu et al., 2005). Constituents of ultrasound probes such as the external cover, backing region, matching layer and piezo electric materials contain metals of alloys of metals and epoxy resin (Zhou et al., 2014) likely to interfere with gamma-rays. However, as the exact compositions of ultrasound probes are not provided by manufacturers, the effects of their presence in the PET field of view (FOV) cannot be reliably estimated using models. Therefore, it is necessary to investigate experimentally these effects on image quality and, since PET is a quantitative molecular imaging modality, to appreciate their influence on measurements of tissue radioactivity concentrations.

Here, we investigated the effects of static or mobile ultrasound probes inside the PET gantry on the quality of PET images. We performed tests under the conditions described by the National Electrical Manufacturers Association (NEMA) NU 4-2008 standard (National Electrical Manufacturers Association, 2008) protocol for small-animal PET systems. Then, we investigated the effects of ultrasound probes on the quantification of in vivo dynamic studies of 2-deoxy-2 [^{18}F] fluoro-D-glucose (FDG) uptake in beating mouse and rat hearts.

2. Methods and Materials

2.1 Petrus system description

The PETRUS system (Fig. 1) combines a compact preclinical PET-CT system for small animals (nanoScan PET/CT, Mediso Ltd., Hungary) with a clinical UUI scanner (Aixplorer, Supersonic Imagine; Aix-en-Provence, France) connected to different ultrasound probes (Figure 1 B, C and D). The PET system is made of 12 blocks of detectors of 39×81 scintillator crystal arrays of Lutetium Yttrium OrthoSilicate:Cerium (LYSO:Ce) elements, with a pitch of 1.17 mm. Different sets of blocks can be put in coincidence for trade-off between spatial resolution, sensitivity, and dimension of the field of view (FOV) in order to cover a wide variety of scenarios. The possible coincidence configurations are 1:1, 1:3 and 1:5, covering an axial FOV of 94 mm by respectively 45, 94 or 120 mm transaxially. Crystals are arranged in 81 rings, comprising a total of 37908 crystals within a ring diameter of 184 mm and they are coupled to two multi-anode position-sensitive photomultipliers (H9500; Hamamatsu) and an optimized thin light guide is used to identify the individual crystals in the arrays.

List-mode format is employed to store the events (both prompts and delayed) that are processed in real time during the acquisition and stored with their coordinates, energy and time-stamp information. Single-slice rebinning (SSRB) allows binning the list-mode data into 2-dimensional (2D) sinograms or line-of-response files. The available reconstruction modalities are: filtered-backprojection (FBP), ordered-subset expectation maximization (OSEM) (Alessio and Kinahan, 2006) and the Tera-Tomo 3D method (Tera-Tomo^{TM} 3D, Mediso, Hungary), a fully 3-dimensional (3D) reconstruction algorithm based on penalized maximum-likelihood and total variation regularization. The main technical characteristics of this system are shown in Table 1. For extensive description of the NanoScan PET/CT, see (Major et al., 2009, Szanda et al., 2011).

The UUI component of PETRUS operates in ultrafast image acquisition mode up to 10,000 images per second, allowing the exploration of rapid phenomena and with very high sensitivity. Ultrafast ultrasound has a rapidly growing field of applications, and can be used in multiple modes within the PETRUS system, such as ultrafast Doppler for imaging the microvasculature of tumors, Shear-Wave Imaging to map tissue stiffness, and B-mode imaging for the mapping of anatomy (Provost et al., 2018).

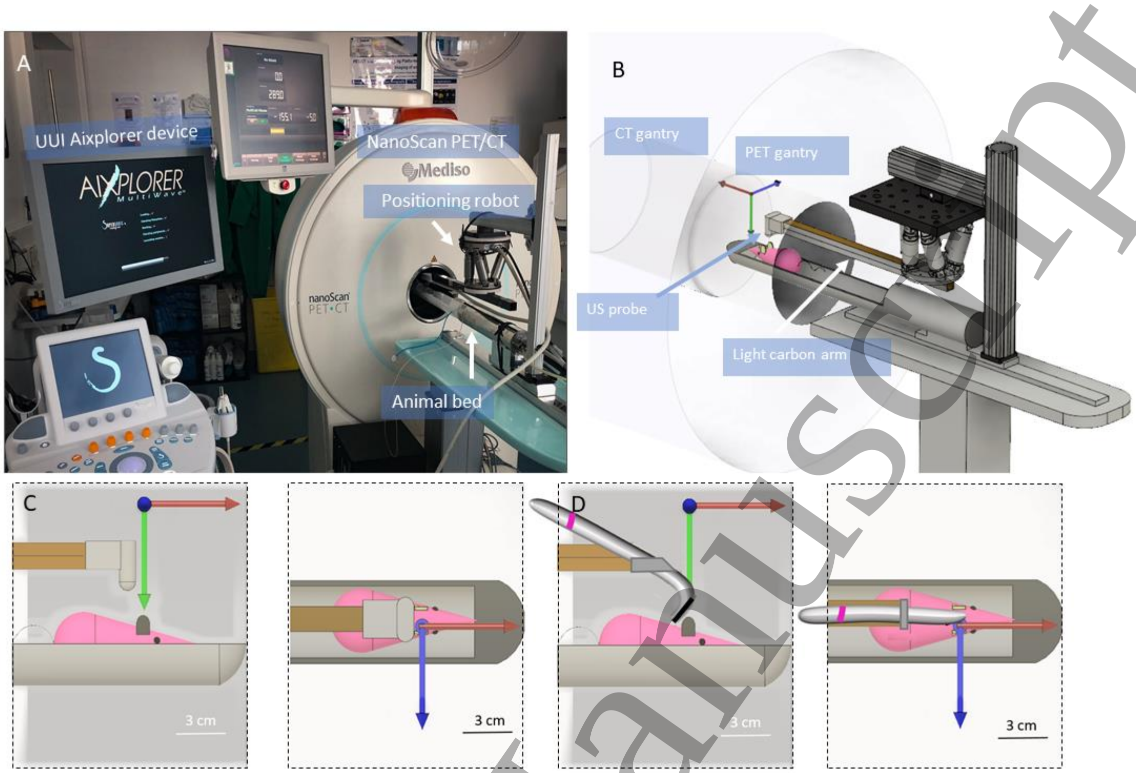

Figure 1. Description of the PETRUS imaging instrument. **A**- Photograph of PETRUS setup. **B**- Schematic representation of the PET/CT system showing position of ultrasound probe and animal. **C-D** Schematic representation of the lateral and superior view of the PET gantry with the *mouse* probe (**C**) and the *rat* probe (**D**). Dashed black lines in C and D indicate the limits of the PET gantry.

In order to image the microvascular network in mice bearing tumors, PETRUS uses a custom-made ultralight probe (Vermon, France; Figure 1 B and C) with 15 MHz central frequency, 128 transducer elements and 100 µm pitch, referred to as the *mouse* probe in the text. Concerning cardiac studies in rats, for which a deeper imaging depth is required, PETRUS is connected to a commercial pediatric/rheumatology probe (SuperLinear™ SLH20-6, Supersonic Imagine, France; Figs. 1 D) with 12 MHz central frequency, 192 transducer elements and 140 µm pitch referred to as the *rat* probe.

Both probes are attached to the system through a 35-cm long hollow carbon rectangular cuboid (Polyplan Composites, France) to a six-degree-of-freedom high-precision micromotor (Hexapod H811, Physik Instrumente, Germany; minimum incremental motion = 0.2-µm) fixed to the animal bed of the PET/CT scanner. The motion range of the probe inside the PET gantry covers an area of 36 × 40 × 40 mm^3. Acoustic impedance coupling between the probes and the skin of the animals is obtained by degassed ultrasound gel (Medi'gel Blue ECG, Drexco Medical). To study xenograft tumors in mice an ultralight water pool interposed between the probe and the gel is also employed, as described in (Provost et. al, 2018).

Table 1. Technical characteristics of the nanoScan PET/CT system (Mediso Ltd., Hungary)

	Properties	**Descriptions**
Detectors Characteristics	Crystal material	LYSO
	Crystal size (mm)	1.12 × 1.12 × 13.00
	Pitch (mm)	1.17
System Characteristics	Total number of crystals	37908
	No. Of blocks	12
	No. Of rings	81
	Ring diameter (mm)	184
	Crystals per ring	468
	Coincidence mode	1:1, 1:3, 1:5
	Axial FOV (mm)	94
	Transaxial FOV (mm)	45, 94, 120
	Spatial res. (mm)	0.7*/1.2**
	Temp res. (ns)	1.5 ± 0.2
	Energy res. (%)	19
Dataset Characteristics	Sinograms 2D	161
	Sinograms 3D	6561
	Sinogram size	341 × 341
	Sampling distances (mm)	0.3

* Tera-Tomo^{TM} 3D PET reconstruction engine. ** with FBP according with NEMA standards.

2.2. NEMA protocol tests

We performed all four types of tests recommended by the NEMA NU 4-2008 standard protocol (National Electrical Manufacturers Association, 2008, see Appendix A for an extensive description): (1) Spatial resolution, (2) Scatter fraction, count losses and random coincidence measurements**,** (3) Sensitivity and (4) Image quality, accuracy of attenuation and scatter corrections. For tests (1) and (3), we used a ^{22}Na point source (0.25 mm sphere centered in a 1 × 1 × 1 cm cast acrylic cube; MMS09 022-25U, Eckert-Ziegler Isotope Products GmbH). For test (1), we analyzed the effect of the presence of the probe at two axial positions in the axial axis of the PET gantry and at several radial and axial distances (0, 5, 10, 15 and 25 mm). To mimic a typical acquisition in PETRUS, the probe was oriented as shown in Fig. 1 with the source underneath representing the PET/CT-UUI volume of interest, and both were moved together. To analyze spatial resolution in regions distant from the VOI situated underneath the probe, the probe was fixed in the center of the FOV, positioned and aligned as in Fig. 1, and the source was moved 0, 5, 10, 15 and 25 mm-distance in the radial and axial directions. For test (2), we employed a mouse-like phantom (Micro-PET NEMA-NU4 Mouse like QRM-MicroPET Scatter Phantom; QRM Quality Assurance in Radiology and Medicine GmbH, Germany) and a rat-like phantom (Micro-PET NEMA-NU4 Rat like QRM-MicroPET

Scatter Phantom; QRM Quality Assurance in Radiology and Medicine GmbH, Germany). For test (3), we mounted the ^{22}Na source over the animal bed and moved it together with the probe along the axial axis of the scanner. For test (4), we employed a NEMA Image Quality (IQ) phantom (Mediso Ltd., Hungary). In all cases, tests were performed with and without the presence of the probes in the PET FOV. For tests (1), (2) and (3) data were sorted into sinograms of 161 slices using 2D-SSRB, without softening or corrections, with a ring span of 81, coincidence window of 5 ns and Filtered Back Projection (FBP) reconstruction. The pixel size and slice thickness of the reconstructed images were 0.3 mm and 0.585 mm respectively. For test (4), we used the whole-body Tera-Tomo 3D reconstruction method with 4 iterations and 1 subset and we corrected by attenuation, decay, scatter and random events. This resulted in images of $155 \times 210 \times 222$ voxels with a voxel size of $0.4 \times 0.4 \times 0.4$ mm^3. For test (4), the energy window span used was 400-600 keV, while for tests (1), (2) and (3), the energy window span used was 250-750 keV (as in reference Szanda et al., 2011). In cases for which the NEMA protocol requires performing calculations over particular parts of the phantoms, for example in the image quality test, the probes were located above the related section of the phantom (see Fig. 4).

2.2 In vivo measurements

To test the effect of the presence of the probes in the PET-FOV in realistic in vivo experiments, we performed PET acquisitions in two rodents (one mouse and one rat) placed in the PET-FOV with and without the ultrasound probe. Animals were anesthetized with 2% isoflurane under constant monitoring of body temperature, electrocardiogram and respiration and the respective probe was placed just above the heart of the animal. Animals were injected through the tail vein with a tracer dose of FDG (6.5 MBq for the mouse and 62 MBq for the rat) and a series of sequential 5-minutes acquisitions was started immediately, alternatively moving the probe in and out the PET-FOV. Using the computer-controlled positioning micro-motor we ensured that the probes returned to the exact same position over the heart of the animal after each acquisition. Overall, 14 acquisitions alternating consecutive with/without probe (7 with probe and 7 without probe) were acquired.

Each PET acquisition was reconstructed using the whole-body Tera-Tomo 3D method using 4 iterations and 1 subset, a coincidence mode 1:5, a 400-600 keV energy window and CT-based attenuation correction. Data was corrected for decay time, attenuation, random and scatter. Image analysis was performed using PMOD software package (PMOD Technologies Ltd, Zürich, Switzerland) by segmenting the heart of the animal in 3D isocontours at 35% of the maximum voxel value.

3 Results and discussion

3.1 Spatial resolution

Figure 2 shows the transaxial (Fig. 2 A and B) and axial (Fig. 2 C and D) spatial resolutions with and without the ultrasound probes, at the center of the FOV (Fig. 2 A and C) and off-center at one fourth the axial length of the FOV (Fig. 2 B and D). At the center of the FOV, the Full Width at Half Maximum (FWHM) in the absence of the probe varied from 1.46 mm to 2.75 mm at the maximum radial distance explored (25 mm). The corresponding results in terms of the Full Width at Ten percent of the Maximum (FWTM) where 2.67 and 5.39 mm. In the presence of the mouse probe, when probe and source were located at several position inside the PET gantry, the FWHM varied from 1.47 to 2.90 mm and the FWTM from 2.70 to 5.57 mm. In same conditions, with the rat probe, FWHM and FWTM varied from 1.48 to 2.94 mm and from 2.74 to 5.87 mm, respectively. Similar results were obtained off-center at one fourth the axial length of the FOV, where the FWHM varied from 1.46 to 2.82, from 1.53 to 2.85 mm and from 1.50 to 3.02 mm for the no-probe, mouse probe and rat probe cases respectively. Regarding the FWTM, the resolution varied between 2.65 to 5.14 mm, from 2.80 to 5.20 and from 2.73 to 5.67 mm for the no-probe, mouse probe and rat probe cases respectively.

On the other hand, the values measured for both the FWHM and the FWTM at the center of the FOV and at one fourth of the FOV off-center remained practically constant along the axial profiles measured in those positions. This is in agreement with previously reported values for the Mediso NanoScan PET/CT (Nagy et al., 2013, Szanda et al., 2011). The biggest discrepancies were found for farther radial and axial distances from the center of the scanner FOV, as the sampling is less homogeneous towards the walls and extremities of the scanner.

When the probe was fixed in the center of the FOV and the source was moved to different radial and axial off-center positions, the presence of the probe degraded the spatial resolution more in the radial direction than in the axial direction. Loss in spatial resolution was also dependent on the distance from the source to the probe. In the axial direction, resolutions at 25 mm off-center with the mouse probe were 1.63 mm and 3 mm for the FWHM and FWTM respectively, and 1.7 mm and 3.3 mm for the FWHM and FWTM respectively at 25 mm off-center with the rat probe. In the radial direction, FWHM and FWTM resolutions at 25 mm off- center were respectively 3 mm and 5.8 mm with the mouse probe and 3.2 mm and 6.4 mm with the rat probe.

Overall the presence of the probe in any of the positions tested led to a loss in resolution of less than 7 % for the mouse probe and approximately 10 % for the rat probe. The smaller influence of the smaller mouse probe on resolution highlights the importance of miniaturizing probes as much as possible for optimized PETRUS settings. The use of this small-sized costume-made probe carries out a reduction in the amount of high atomic number material inside the FOV, which at the given energy of the PET photons will cause mostly scatter-type interactions and affect the random events estimation (Berger et al., 2010) that appear as the cause of the degradation of the resolution.

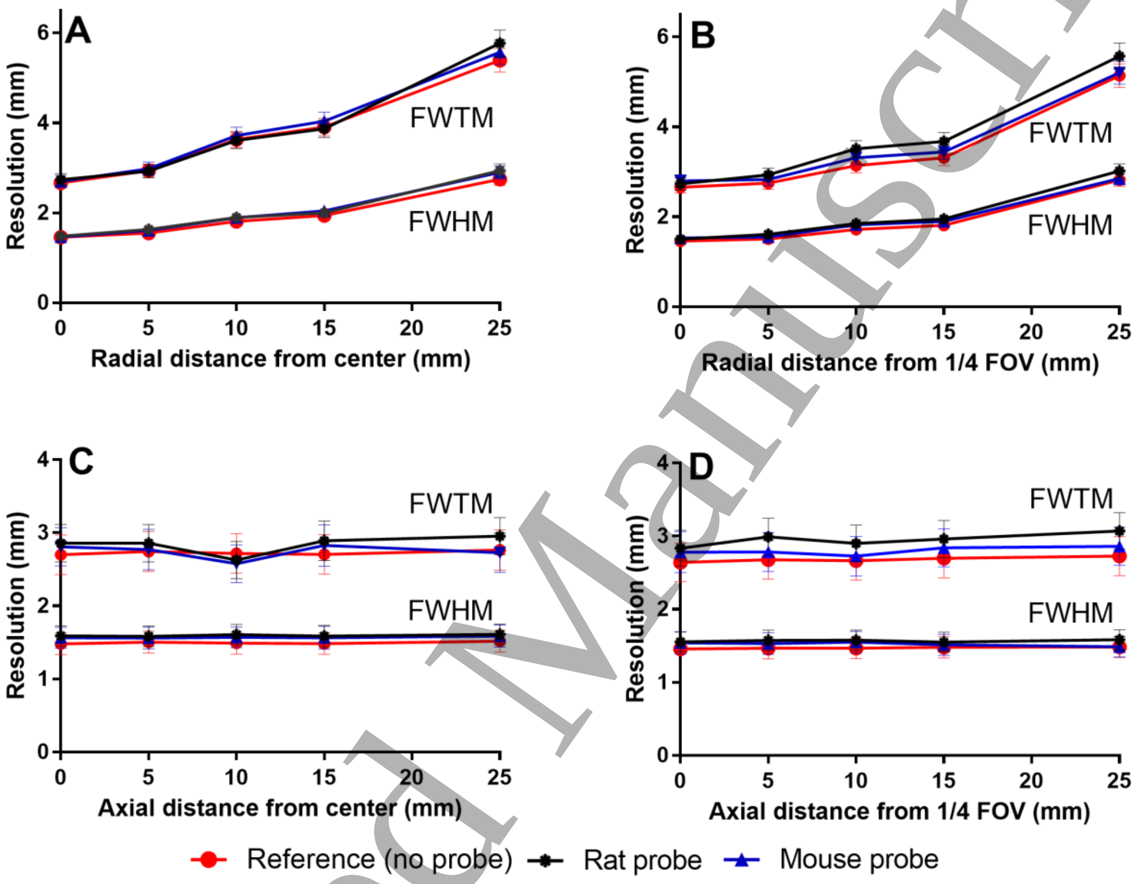

Figure 2. Effect of the presence of the ultrasonic probes on the spatial resolution using a ^{22}Na point source placed at two axial positions; at the center of the FOV and at an offset one fourth of the size of the FOV. In both positions, acquisitions where taken at 0, 5, 10, 15 and 25 mm radial and axial distances from these two locations (see Appendix A). **A-** transaxial resolution at the center of the field of view (FOV) **B-** transaxial resolution at one-fourth of FOV. **C-** depicts the axial resolution at the center of the FOV and **D-** axial resolution measured at one fourth length of the FOV. Lower curves in all plots refer to FWHM and upper curves refer to FWTM.

3.2 Scatter fraction (SF), Count losses (CL) and Noise equivalent count (NEC)

In mouse-like standard NEMA conditions, i.e. no probe in the FOV, using an energy window of 250-750 keV, the NEC peak was achieved with an activity concentration of 0.129 MBq/cc with 239 kcps (Fig. 3 A).

The presence of the mouse probe slightly modified the position of this peak to an activity concentration of 0.112 MBq/cc and the number of counts detected to 234 kcps. Similar results were obtained in the rat-like configuration (Fig. 3 B): in NEMA-standard probe-free conditions, the NEC peak was at an activity concentration of 1.06 MBq/cc with 99 kcps, and with the probe in the FOV, the NEC peak was at 0.97 MBq/cc with 87 kcps.

The true count-rate peak using the mouse-like configuration was at an activity concentration of 0.133 MBq/cc with 332 kcps without any probe, and at an activity concentration of 0.116 MBq/cc with 333 kcps with the mouse probe in the FOV (Fig. 3 A). The true count-rate peak using the rat-like configuration was at 1.118 MBq/cc with 162 kcps without probe and at 1.088 MBq/cc with 145 kcps with the rat probe in the FOV (Fig. 3 B). The calculated scatter fractions were 20% and 22% for the mouse-like NEMA-standard configuration with and without the probe, respectively (Fig. 3 A). The scatter fractions in the rat-like configuration were 33 % and 37% without and with rat probe, respectively (Fig. 3 F). On average, discrepancies in the NEMA-standard measurements induced by the presence of the probe in the PET-FOV were under 5 % for the mouse-like configuration for all the parameters investigated. Discrepancies induced by the presence of the probe in the PET-FOV were somewhat higher in the rat-like configuration, up to ~20 % at some activity concentrations. However, the higher discrepancy in the rat-configuration is also a consequence of the fact that part of the rat phantom did not fit inside the gantry, and therefore, scatter events from outside the FOV of the scanner also contributed to the events calculation.

3.3 Sensitivity

Fig. 3 C shows plots of the absolute sensitivity of the scanner along the axial distance. In NEMA-standard no-probe configuration, the maximum value at the central axial and transaxial location of the scanner was measured at 7.6 %, which is consistent with previously reported values for the Mediso NanoPET/CT scanner (Nagy et al., 2013). The presence of probes inside the scanner FOV introduced small variations in these curves, with an absolute sensitivity peak equal at 7.5 % and to 6.8 % with the mouse and rat probe, respectively. For all the positions measured, the maximum discrepancies between the measurement without and with probe in the FOV was 2.7 % and 6.7 % for mouse and rat, respectively. The modification of the total sensitivity (S_{tot}), the total sensitivity of the mouse-like and rat-like configurations ($SM_{tot}$and SR_{tot}, respectively), the absolute sensitivity for the standard, mouse-like and rat-like configurations (S_A , SM_A and

SR_A , respectively) with and without the presence of the probe are shown in Table 2. The presence of the probes had not relevant effect on any of these parameters.

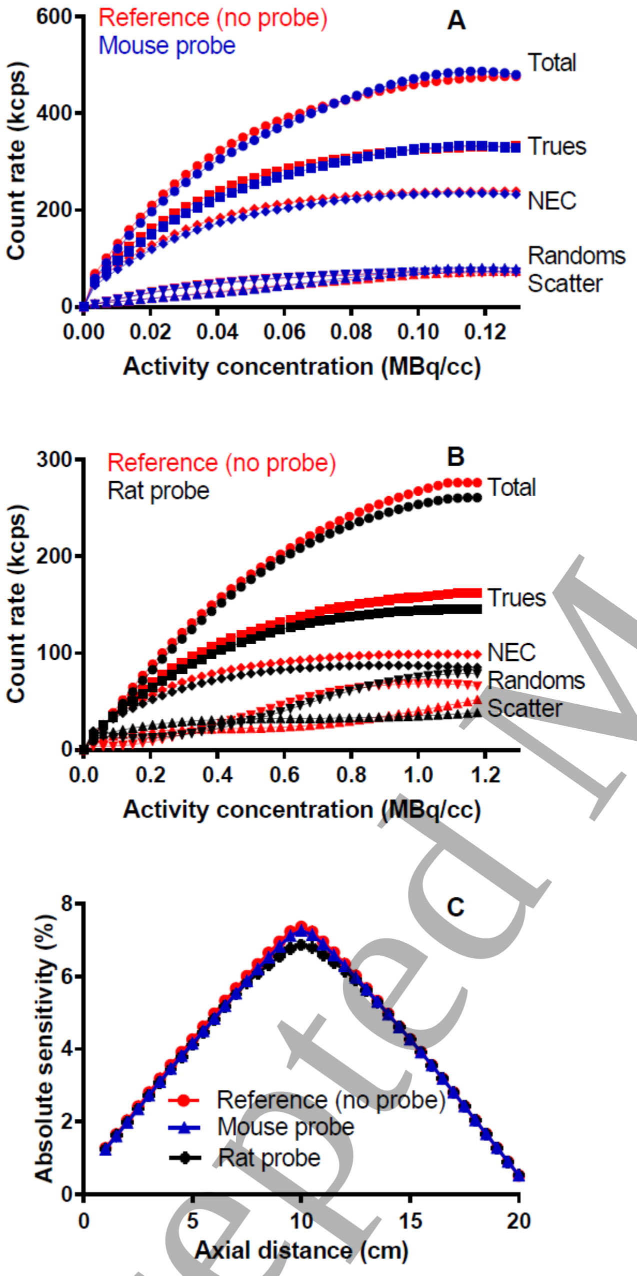

Figure 3. Total, true, random, scattered and noise-equivalent count-rate (NEC) events as a function of the injected activity in the phantom for the **A**- Mouse-like configuration and **B**- Rat-like configuration. **C**-depicts the absolute system sensitivity profiles. In all cases reference standard NEMA results are shown in red, and the results with the mouse and rat probes are plot in blue and black respectively.

Table 2 Total (S_{tot}) and absolute (S_A) sensitivity calculations for the scanner and for the mouse-like and rat-like configuration of the scanner. The effect on these parameters of the presence of the mouse (M) and rat (R) probes is also reported

	No probe	**Mouse probe**	**Rat probe**
S_{tot} (kcps/MBq)	7.6	7.5	7.4
SM_{tot}(kcps/MBq)	4.1	4.1	4.1
SR_{tot}(kcps/MBq)	7.6	7.5	7.5
S_A (%)	4.2	4.1	4.0
SM_A (%)	6.4	6.4	6.2
SR_A (%)	4.2	4.1	4.0

3.4 Image quality, accuracy of attenuation, and scatter corrections

Figures 4 and 5 show the results of the NEMA image quality test. In Fig. 4, we can see the fusion of the CT and reconstructed PET for the configurations with and without probes. No relevant artifacts or strong degradation of the image quality is observed for any of the configurations studied. Fig. 5 shows the quantitative results obtained for the image quality test. Regarding the uniformity test (Fig. 5 A), the effect of the presence of any of the probes in the uniform region induced no substantial change. The uniformity value under the reference conditions was 0.3 MBq/ml in all cases, including in conditions in which the probes were moved along the phantom during the PET acquisition. Interestingly, attenuation correction in conditions of moving probes showed that acquiring just one CT-scan with the ultrasound probe in its starting position has a negligible effect, since the differences in the results with the static-probe and the moving-probe studies below were 3 %. Therefore, this strategy can be used for attenuation correction in PETRUS when dynamic ultrasound scans are employed, without a significant loss in the sensitivity of count detection in the images.

Discrepancies in the recovery coefficients (RC) from the hot rods of the phantoms (Fig 5 C) between reference NEMA-standard RC and RC measured with probes inside the PET gantry were below 4% and 7% for mouse and rat probes, respectively. Noise (Fig. 5 B), calculated as the ratio of the standard deviation and the mean value in the region of interest (ROI), was 8.60 %, 8.64 % and 8.90 % for the reference NEMA-standard, mouse and rat probes configurations, respectively. For dynamic ultrasound studies, noise values were 8.7 % and 9 % for the mouse and rat probes, respectively. The spill-over calculation (Fig. 5 D) showed discrepancies under 10% between the different configurations. Again, these values are in agreement with previously reported results for the NanoScan Mediso scanner (Szanda et al., 2011, Nagy et al., 2013).

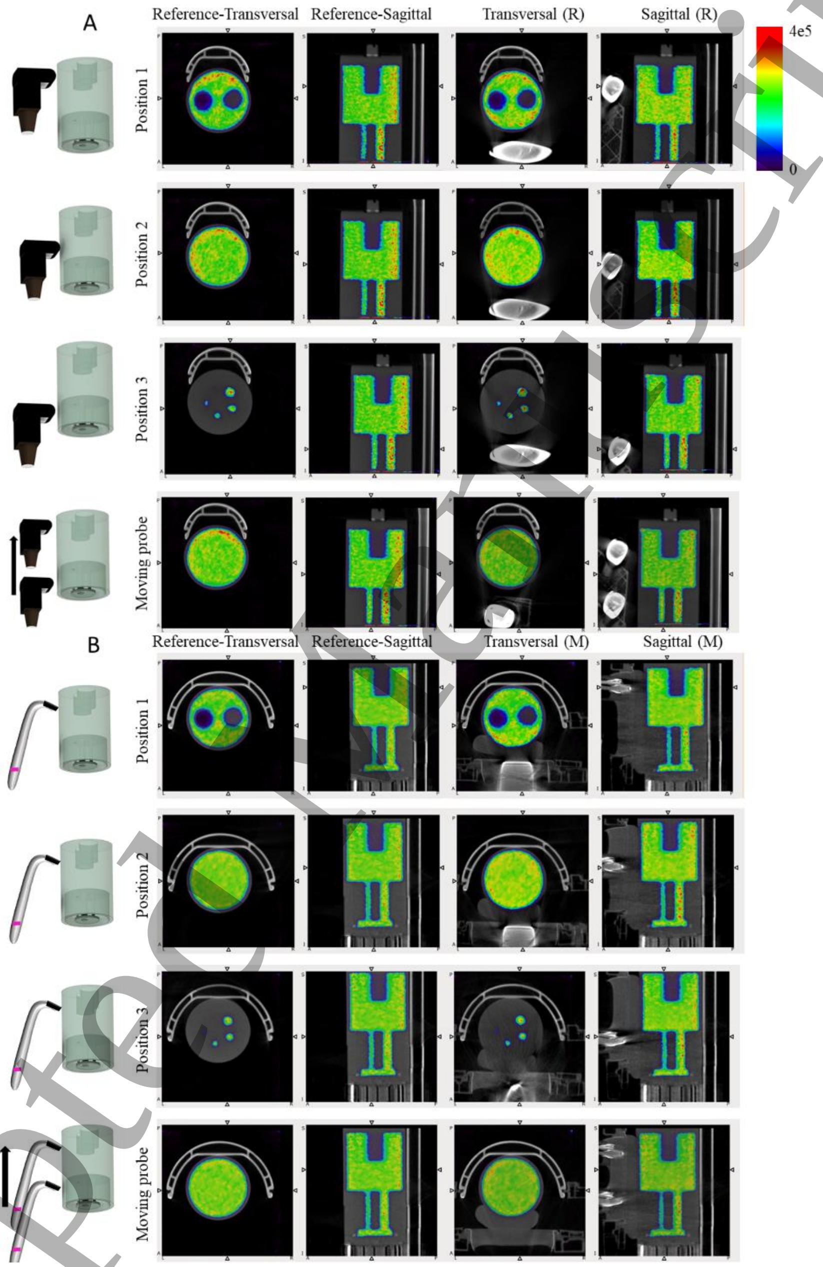

Figure 4. PET/CT fusion images of the image quality phantom. The drawings on the left indicate the position of the mouse (panel **A**) and rat (panel **B**) probes with respect to the phantom. CT is shown in gray scale and PET in NIH color scale. The two left columns depict the transversal and sagittal views of the phantom under reference conditions, i.e. no probe in the PET gantry, and the two right columns represent the acquisitions with probes (visible in the images) located over the different parts of the phantoms: (i) over

the cold region: top row in panels A and B, (ii) over the homogeneity region: second to top row in panels A and B; (iii) over the rods region: third row off panels A and B; (iv) moving probe: bottom row of panels A and B.

3.4 In vivo measurements

Images were acquired in mouse and rats one hour and a half after injection of FDG with and without probes positioned over the cardiac notch. At these time points, the cardiac uptake of FDG in rodents is at a plateau and the 5 min difference in image acquisition times is unlikely to be significant. As shown in Fig. 6 the quality of the images with and without probe are similar in the organ of interest, in this case the heart, and in other organs in the FOV, demonstrating that the presence of the probe has no real influence on visual image inspection. To determine whether this is also true for quantification of FDG uptake in organs, time-activity curves (TAC) in volumes of interest covering the heart of the animals were drawn. Fig. 7 clearly shows that, at any time point during cardiac FDG uptake, the TACs with and without probe were essentially superimposable in both species. The maximal mean discrepancies between the TAC with and without probe in mouse and rat were under 2 % and 10 %, respectively.

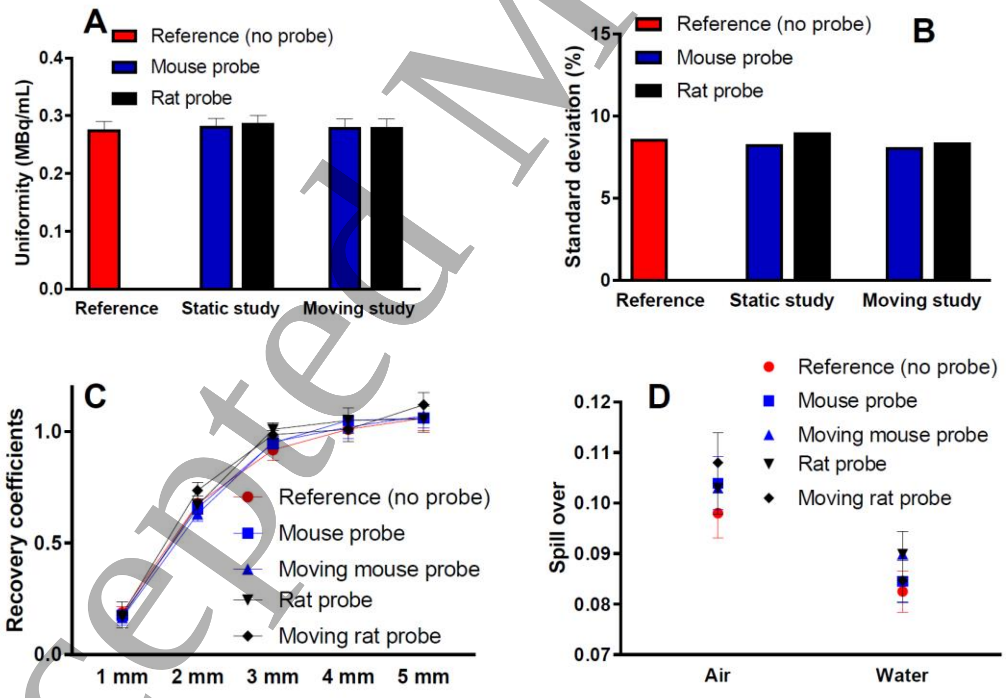

Figure 5. Image quality test of NEMA protocol. Comparison with and without probes in the FOV and for static and dynamic ultrasound scans taken during PET acquisitions. **A**-Uniformity test**, B**-Noise plots**, C**-Recovery coefficients and **D**-Spill-over calculations.

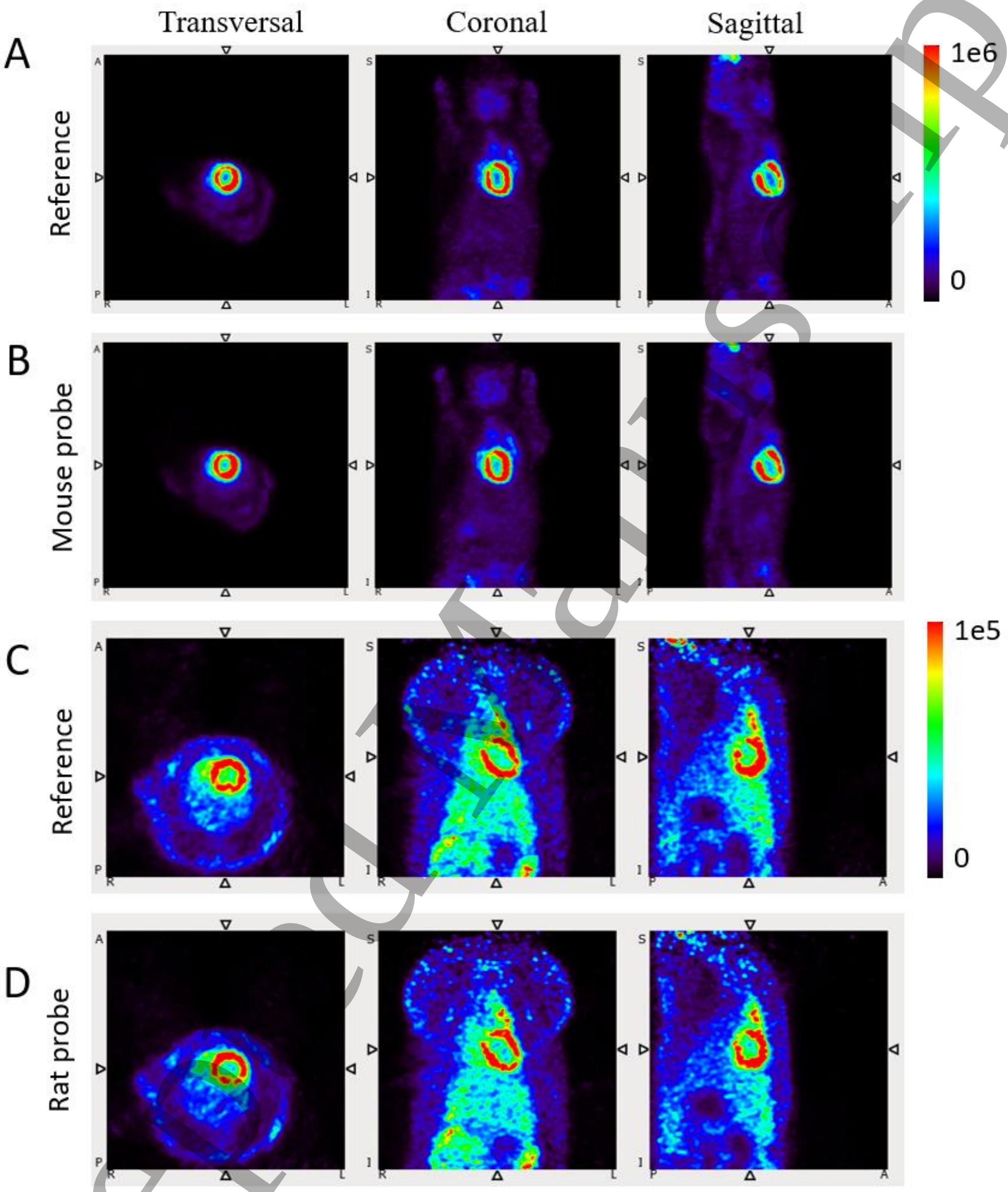

Figure 6. FDG uptake in a mouse **A-** without probe (reference) and **B** with the probe over the heart of the animal and in a rat **C** without probe (reference configuration) and **D** with the rat probe over the heart of the animal. All images show reconstructed 5-minute acquisitions obtained after FDG injection at 83 and 90 minutes for the configurations with probe and without probe, respectively.

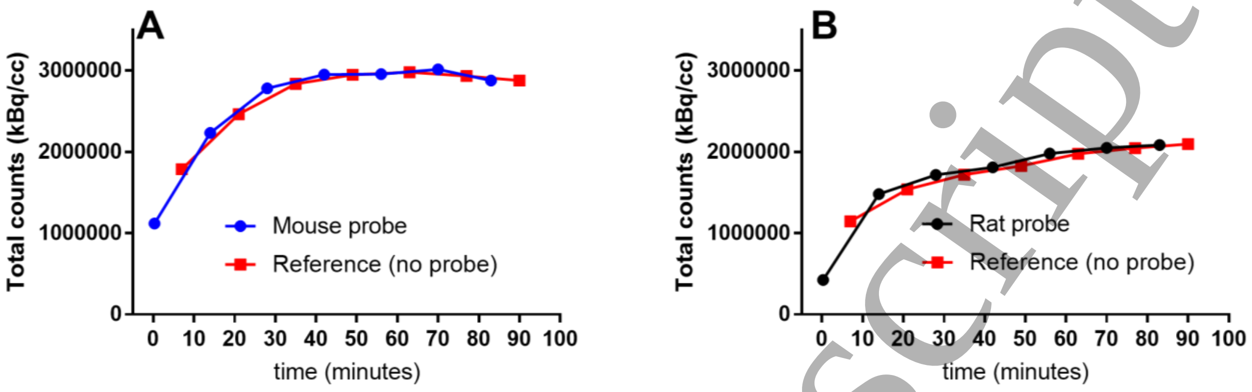

Figure 7. FDG uptake in rodents**. A-** Mouse under a PETRUS acquisition with the *mouse* probe located over the heart compared with its reference without probe and **B-** Rat under a PETRUS acquisition with a rat probe located over the heart compared with its reference without probe.

4 Conclusions

The presence of a UUI probe inside the FOV of the nanoScan PET/CT has a minor effect on the radioactivity concentration measurements in PET images, and does not degrade significantly the quantitative and qualitative PET data derived from the images. Typical maximal discrepancies induced by the presence of the probe in the FOV were under 10 % with the rat probe and under 7 % with the mouse probe, both in the full NEMA in vitro protocol and in in vivo experiments. It is noteworthy that the custom made ultralight probe had a smaller effect on image quality than the commercial one, suggesting that careful design of next-generation miniaturized probes will render them even more stealthy. Compared with the significant advantages of simultaneous UUI and PET acquisitions that offer the unique possibility to co-register metabolism, vascularization, tissue elasticity and anatomy with a low-cost add-on, the PET/CT-UUI device is a remarkable means to increase the range of services offered by molecular imaging with PET.

Appendix A.

A.1 Spatial resolution

This test estimates the spatial resolution defined as the minimum distance at which two point-sources can be acquired and interpreted as disentangled points (National Electrical Manufacturers Association, 2008). The width of the reconstructed point spread function (PSF) from a point source acquisition was characterized as its full width at half maximum (FWHM) and its full width at 10 % of the maximum (FWTM).

A ^{22}Na point source (0.25 mm sphere centered in a 1 x 1 x 1 cm cast acrylic cube; MMS09 022-25U, Eckert-Ziegler Isotope Products GmbH) was placed at two axial positions; at the center of the FOV and at an offset one-fourth of the size of the FOV. In both positions, acquisitions where taken at 0, 5, 10, 15 and 25 mm-distance from these two locations in the radial and axial directions. In all cases both the source and the probe were moved together ensuring the source was located underneath the probe. At each position, measurements were taken during five minutes and list-mode data were acquired in 1:5 coincidence mode. All acquisitions were performed in standard NEMA conditions (1) without probes in the FOV, and with (2) the mouse and (3) the rat probe placed over the ^{22}Na source. A second set of measurements was done with the probes located centered axially and transaxially as in Figure 1, and the source moving. The same axial and radial positions were scanned.

Data were sorted into sinograms of 161 slices using two-dimensional single slice rebinning (2D-SSRB) and a ring span of 81. We used an energy window of 250-750 keV and a coincidence window of 5 ns. Data were reconstructed using the FBP method without softening or corrections. The pixel size and slice thickness of the reconstructed images were 0.3 mm and 0.585 mm, respectively. The PSF width was measured by computing the response functions through the peak of the image in each dimension and fitting to obtain the FWHM and FWTM.

A.2 Scatter fraction, Count losses, and Noise equivalent count

Two phantoms made of high-density polyethylene were employed: (i) a mouse-like phantom (Micro-PET NEMA-NU4 Mouse like QRM-MicroPET Scatter Phantom; QRM Quality Assurance in Radiology and Medicine GmbH, Germany) made of a solid circular cylinder 70 mm long and 25 mm in diameter with a cylindrical hole of 3.2 mm diameter at a radial distance of 10 mm from the central axis of the cylinder; (ii) a rat-like phantom (Micro-PET NEMA-NU4 Rat like QRM-MicroPET Scatter Phantom; QRM Quality Assurance in Radiology and Medicine GmbH, Germany) made of a solid circular cylinder 150 mm length and 50 mm in diameter with a cylindrical hole 3.2 mm in diameter at a radial distance of 17.5 mm from center.

The holes contained a flexible tube filled with FDG. The phantoms were placed in the animal bed longitudinally, i.e. parallel to the axial axis and in the center FOV of the scanner. Four acquisitions were taken with each of the phantoms following the standard NEMA protocol and then repeated with the transducing probe located over the middle of their larger axis and transaxially centered in the PET-FOV.

The FDG activity in the part of the rat-like phantom that could be acquired in the 94.8 cm axial FOV of the scanner was 42 MBq. Note the axial length of this phantom exceeds the length of the FOV of the scanner. For the mouse-like phantom, the FDG activity was 37 MBq. Two-minute long acquisitions were repeated every 10 minutes during 8 hours. As the scanner's crystals contain ^{176}Lu that can affect the trues count-rate measurements, background measurements of 20 minutes with both phantoms without activity were also taken.

Data was sorted into sinograms of 161 projections with 0.3 mm pixel size and 0.585 mm pixel thickness, using 2D-SSRB and maximum ring difference of 81, an energy window of 250-750 keV, a coincidence window of 5 ns and 1:5 coincidence mode. No data corrections were used. Sinograms were aligned to center the pixels of maximum activity at each projection angle and after that, all projections from each slice and each acquisition were added.

We computed the random plus scattered events $C_{r+s,i,i}$ at each slice *i* and acquisition frame *j*. This value was calculated as the sum of two terms: (1) the product of the average pixel intensity at both edges of a 14 mm wide strip located at the center of the sum projection times the number of pixels between these edges; (2) the counts in the pixels outside the strip. Using this value and the total events counts $C_{TOT,i,j}$ (sum of all values in the sum projection of slice *i* and acquisition *j*) the true event rate $R_{T,j}$ at each frame is:

$$R_{T,j} = \sum_i \frac{C_{TOT,i,i} - C_{r+s,i,i}}{T_{acq,j}} \tag{1}$$

where $T_{acq,j}$ is the acquisition time for frame *j*.

Using the last frame, the scatter fraction of the system is:

$$SF = \sum_i \frac{\sum_j C_{r+s,i,j}}{\sum_j C_{TOT,i,j}} \tag{2}$$

Using this expression, the rate of detection of random events $R_{r,j}$ in each frame was calculated as:

$$R_{r,j} = \sum_i \left[R_{TOT,i,j} - \left(\frac{R_{T,i,j}}{1 - SF_i} \right) \right] \tag{3}$$

and the rate of scattered events is given by:

$$R_{s,j} = \sum_i \left[R_{TOT,i,j} - R_{T,i,j} - R_{r,i,j} - R_{int,i} \right] \tag{4}$$

where $R_{int,i}$ is the intrinsic true count rate of the scanner obtained as a background measurement.

Finally, the NEC is:

$$R_{NEC,j} = \sum_i \frac{R_{t,i,j}^2}{R_{TOT,i,j}} \tag{5}$$

The values for all parameters were plotted against the activity concentration, allowing to derive parameters such as: peak true count rate $R_{t,peak}$, peak noise equivalent count rate $R_{NEC,peak}$, the activity concentration at which $R_{t,peak}$ is reached $a_{t,peak}$, the activity concentration at which $R_{NEC,peak}$ is reached $a_{NEC,peak}$ and the system scatter fraction (SF). All values were compared with and without the presence of the ultrasound probes in the PET-FOV.

A.3 Sensitivity measurements

The aim of this test is to determine the rate of true coincidence events detection in the scanner in counts per second (cps). The same ^{22}Na source used in section A.1 was placed in the animal bed axially and transaxially centered in the FOV. The source was moved using the animal bed along the axial FOV of the scanner towards both edges of the FOV. List-mode data was acquired for one minute at each location in 1:1 coincidence mode, with an energy window of 250-750 keV and a coincidence windows of 5 ns.

To account for the intrinsic background events of the scanner, we collected 20 minutes' acquisition with no source in the FOV. The rest of measurements were taken first using the standard NEMA setup with only the source inside the PET-FOV and posteriorly, they were repeated with each of the probes investigated, by moving them simultaneously with the source movements.

Data was sorted in sinograms using 2D-SSRB where all pixels situated farther than 1 cm from the maximum pixel of each raw masked to zero. The ring span used was 81 and no data corrections were employed.

From the masked sinograms, the total count rate R_i at each position i was calculated as the counts in the sinograms divided by the time of acquisition. Using this value and the background count rate $R_{B,i}$, the sensitivity of the system at each position was :

$$S_i = \frac{R_i - R_{B,i}}{A_{cal}} \tag{6}$$

where A_{cal} is the calculated activity of the source, in our case 0.41 MBq at the time of the measurement. No loss of sensitivity due to photon attenuation with the plastic cover of the source was considered. Taking a branching ratio of 0.9060 for the ^{22}Na source, the absolute sensitivity at each slice was:

$$S_{A,i} = \frac{S_i}{0.9060} \times 100 \tag{7}$$

According to the NEMA protocol, this test should report the total system's sensitivity $S_{tot} = \sum_i S_i$ (without probe), the system sensitivity for mouse SM_{tot} and rat SR_{tot} applications, that can be calculated by adding all the slices of the sinograms comprising the central 7 cm and 15 cm of the FOV of the scanner. However, for our scanner the length of the FOV is smaller than 15 cm, therefore the system sensitivity for rat phantoms was calculated by adding all the sensitivity values along the total FOV. The system's absolute $S_A = \sum_i S_{A,i}$, rat SR_A and mouse SM_A sensitivities were also investigated. All values are reported with and without the presence of the probes in the FOV.

A.4 Image quality, accuracy of attenuation, and scatter corrections

Image quality was measured in a standardized situation simulating total body imaging study of a small rodent with different hot and cold areas. Here, the aim of this test was to analyze image quality parameters with probes inside the PET-FOV. All available corrections were employed for these studies, we also analyzed the effect of different positions of the probes on image quality.

The NEMA Image Quality (IQ) phantom (Mediso Ltd., Hungary) made of an heterogeneous polymethacrylate cylinder (50 mm-length, 30 mm-diameter) is divided in three regions: (i) two cold cylinders (15 mm-length and 8 mm-diameter) used to measure the scatter fraction are in the upper part of the phantom: one is filled with non-radioactive water and the other one is filled with air: (ii) to test the recovery coefficients values of the system, the extremity of the phantom contains five 20 mm-long rods of different diameters (1, 2, 3, 4, and 5 mm) with walls thinner than the spatial resolution of the imaging scanner and were filled with a calibrated concentration of FDG; (iii) the central part of the phantom is designed to test the signal-to-noise levels and is made of a homogeneous cylinder connected to the rods filled with the same FDG concentration. All acquisitions were performed with the phantom placed at the center of the FOV aligned along the axial axis of the scanner. Image quality parameters were measured by placing the probes just above the center of the corresponding region, as it is shown in Figure 4. In order to study the effect of a probe moving inside the PET gantry, we performed an additional test in which the probe was moved from the center of the rods' region to the center of the cold region. All acquisitions were repeated in a NEMA reference standardized situation and with the presence of each of the probes, for a total of 4 tests in each configuration. 7.8 MBq of FDG was introduced in the phantom and acquisitions continued until achieving a fixed number of counts (3.7 Mcounts) when the probe was positioned at the center of each region. The same procedure was applied without any probes in the FOV and then with the mouse or the rat probes placed: (1) over the rods region, (2) over the uniform region, (3) over the cold region and (4) or in continuous motion above the phantom (movement duration: 15 minutes).

The list mode data acquired was binned using 1:5 coincidence mode and 400-600 keV energy window. Each set of acquired data was reconstructed using the whole body, Tera-Tomo 3D reconstruction method, with 4 iterations and 1 subset. Attenuation correction and normal resolution were used together with random, scatter and decay corrections. This resulted in images of 155×210×222 voxels with a voxel size of 0.4× 0.4 × 0.4 mm.

Data analysis was performed to extract values of image uniformity (in uniformity region), resolution recovery coefficients (in rods region), and accuracy of data corrections (in cold region). The recovery coefficients measured in hot regions are indicative of the resolution and sensitivity of the system. Noise in the uniform region (background) measures the signal to noise ratio (SNR), while uniformity measurements informs about the accuracy of attenuation and scatter corrections, also obtained from contrast measurements in cold regions.

To measure uniformity, a 22.5 mm-diameter by 10 mm-long cylindrical volume of interest (VOI) was employed. In this VOI, we computed the average activity concentration, the maximum and minimum values, and the standard deviation (%STD).

The recovery coefficients were calculated in the rods regions using circular regions of interest (ROIs) with diameters twice the physical diameter of the rods. These ROIs were applied to the average of 10 cm-length in the regions of the rods in the phantom. Through these maxima, the values measured along line profiles axially oriented were divided by the uniformity previously calculated to compute the recovery coefficients of each rod.

The accuracy of corrections was computed as the spill-over ratio (SOR) in 4 mm-diameter and 7.5 mm-long VOIs defined in the cold regions, as the ratio of the mean value in the VOIs and in the uniform area.

Acknowledgments:

This study was supported by France Life Imaging grant ANR-11-INBS-0006. This work was supported in part by LABEX WIFI (Laboratory of Excellence ANR-10-LABX-24) within the French programme 'Investments for the Future' under reference ANR-10-IDEX-0001-02 PSL. Author MPL would like to acknowledge the support of the Plan Cancer Physicancer programme BIMUPET (C16025KS). In vivo imaging was performed at the Life Imaging Facility of Paris Descartes University (Plateforme Imageries du Vivant), supported by France Life Imaging (grant ANR-11-INBS-0006) and Infrastructures Biologie-Santé. The project also received the support of the Institut National de la Santé et de la Recherche Médicale (Inserm) Technology Research Accelerator in Biomedical Ultrasound.

References

Alessio, A. and Kinahan, P. (2006). "PET image reconstruction," Nuclear medicine, 1-22.

Berger, M. J., Hubbell, J. H., Seltzer, S. M., Chang, J., Coursey, J. S., Sukumar, R., Zucker, D. S., and Olsen, K. (2010). "XCOM: Photon Cross Section Database (version 1.5)," [Online] Available: http://physics.nist.gov/xcom [2018, July 3]. National Institute of Standards and Technology, Gaithersburg, MD.

Beyer, T., Townsend, D. W., Brun, T. and Kinahan, P. E. (2000). "A combined PET/CT scanner for clinical oncology," The Journal of nuclear medicine 8, 1369.

Enderle, J. D., and Bronzino, J. D. (2012). "Introduction to biomedical engineering". Academic press, 1-1272

Errico, C., Pierre, J., Pezet, S., Desailly, Y., Lenkei, Z., Couture, O. and Tanter, M. (2015). "Ultrafast ultrasound localization microscopy for deep super-resolution vascular imaging," Nature 7579, 499.

Goerres, G. W., Ziegler, S. I., Burger, C., Berthold, T., von Schulthess, G. K., & Buck, A. (2003). "Artifacts at PET and PET/CT caused by metallic hip prosthetic material," Radiology, *226*(2), 577-584.

Hasegawa, B. H., Wong, K. H., Iwata, K., Barber, W. C., Hwang, A. B., Sakdinawat, A. E., Ramaswamy, M., Price, D. C. and Hawkins, R. A. (2002). "Dual-modality imaging of cancer with SPECT/CT," Technology in cancer research & treatment 6, 449-458.

Judenhofer, M. S., Wehrl, H. F., Newport, D. F., Catana, C., Siegel, S. B., Becker, M., Thielscher, A., Kneilling, M., Lichy, M. P. and Eichner, M. (2008). "Simultaneous PET-MRI: a new approach for functional and morphological imaging," Nat. Med. 4, 459.

Mace, E., Montaldo, G., Cohen, I., Baulac, M., Fink, M. and Tanter, M. (2011). "Functional ultrasound imaging of the brain," Nature methods 8, 662.

Major, P., Hesz, G., Szlavecz, A., Volgyes, D., Benyo, B. and Nemeth, G. (2009). "Local energy scale map for NanoPET/CT system,", 3177-3180.

Nagy, K., Toth, M., Major, P., Patay, G., Egri, G., Haggkvist, J., Varrone, A., Farde, L., Halldin, C. and Gulyas, B. (2013). "Performance evaluation of the small-animal nanoScan PET/MRI system," J. Nucl. Med. 10, 1825-1832.

National Electrical Manufacturers Association (2008). "Performance measurements of small animal positron emission tomographs," NEMA Standards Publication, 1-23.

Osmanski, B., Pezet, S., Ricobaraza, A., Lenkei, Z. and Tanter, M. (2014). "Functional ultrasound imaging of intrinsic connectivity in the living rat brain with high spatiotemporal resolution," Nature communications, 5023.

Provost, J., Garofalakis, A., Sourdon, J., Bouda, D., Berthon, B., Viel, T., Perez-Liva, M., Lussey-Lepoutre, C., Favier, J. and Correia, M. (2018). "Simultaneous positron emission tomography and ultrafast ultrasound for hybrid molecular, anatomical and functional imaging," Nature Biomedical Engineering 2, 85.

Prince, J. L., & Links, J. M. (2006). "Medical imaging signals and systems". Upper Saddle River, NJ: Pearson Prentice Hall.

Schmand, M., Burbar, Z., Corbeil, J., Zhang, N., Michael, C., Byars, L., Eriksson, L., Grazioso, R., Martin, M. and Moor, A. (2007). "BrainPET: First human tomograph for simultaneous (functional) PET and MR imaging," Journal of Nuclear Medicine supplement 2, 45P-45P.

Sieu, L., Bergel, A., Tiran, E., Deffieux, T., Pernot, M., Gennisson, J., Tanter, M. and Cohen, I. (2015). "EEG and functional ultrasound imaging in mobile rats," Nature methods 9, 831.

Sureshbabu, W., & Mawlawi, O. (2005). PET/CT imaging artifacts. *Journal of nuclear medicine technology*, *33*(3), 156-161.

Szanda, I., Mackewn, J., Patay, G., Major, P., Sunassee, K., Mullen, G. E., Nemeth, G., Haemisch, Y., Blower, P. J. and Marsden, P. K. (2011). "National Electrical Manufacturers Association NU-4 performance evaluation of the PET component of the NanoPET/CT preclinical PET/CT scanner," J. Nucl. Med. 11, 1741-1747.

Tanter, M. and Fink, M. (2014). "Ultrafast imaging in biomedical ultrasound," IEEE transactions on ultrasonics, ferroelectrics, and frequency control, 61(1), 102-119.

Zhou, Q., Lam, K. H., Zheng, H., Qiu, W., & Shung, K. K. (2014). "Piezoelectric single crystal ultrasonic transducers for biomedical applications," Progress in materials science, 66, 87-111.